Memory effect on gas percolation in saturated porous media

Germán Varas[1] and Valérie Vidal[2]

[1]*Instituto de Fisica, Pontificia Universidad Católica de Valparaiso (PUCV), Avenida Universidad 330, Valparaiso, Chile*

[2]*Laboratoire de Physique, École Normale Supérieure de Lyon–CNRS, 46 Allée d'Italie, 69364 Lyon Cedex 07, France*

(Received 14 March 2025; accepted 31 July 2025; published 25 August 2025)

This work investigates the path of gas locally injected and rising through a water-saturated porous medium. Gas migration through the pores network is modeled using a Gaussian distribution of capillary overpressure superimposed on a linear pressure gradient induced by gravity. Previous studies have shown that the superposition of individual gas pathways significantly affects the overall invasion morphology, impacting various practical applications. The originality of the present simulation lies in incorporating the effect of prior pathways on subsequent ones, thereby accounting for the system's memory. The final invasion zone morphology, shaped by multiple gas pathways, is quantified as a function of the memory effect, ranging from a diffusivelike invasion to a meandering progression when the influence of prior paths is substantial. Notably, we find that the probability of revisiting previously occupied sites, which quantifies the tendency of gas to follow an established path, follows a logistic function.

DOI: 10.1103/d19h-6lx1

I. INTRODUCTION

Immiscible fluid flow in saturated porous media is a long-standing problem that has drastic importance not only in fundamental physics, but also in applications. Fluid transport through such heterogeneous media are encountered in natural or industrial processes, ranging from petroleum and chemical engineering, hydrology, soil remediation, and powder metallurgy, to large-scale gas release and its impact on climate [1–7]. Due to the multiscale, heterogeneous nature of the porous media, quantifying and predicting fluid propagation in these environments has remained, up to now, a major challenge shared by many communities, from geosciences to the physics of disordered media [2,8].

A simple approach to model fluid migration through a rigid porous medium is to consider propagation on a two- or three-dimensional network. The nodes of this network are the interstitial pores through which the fluid propagates. The challenge then lies in defining the nodes properties which will drive the fluid invasion. In the absence of gravity or viscous effects, the so-called invasion percolation models became popular to model fluid displacement in rigid porous media [9]. However, the history of modeling propagation on a network is far more ancient. Eden first proposed a simple cellular growth model in 1961 to describe tumor cell proliferation [10]. About two decades later, the pioneering work of Witten and Sanders [11,12] on diffusion-controlled aggregation triggered many works on cluster formation mechanisms [13]. Among these, Mártin *et al*. [14] managed to define a family of models able to interpolate continuously between the Eden model and invasion percolation models, including cluster growth along a privileged direction. Following this trend, physicists have proposed many numerical models of invasion percolation in a gradient, mainly a pressure gradient to account for gravity [15–20]. Under such conditions, percolation pathways of immiscible fluids depend critically on the spatial distribution of pore throats, local capillary overpressure thresholds, and hydrostatic pressure gradients. This leads to two distinct regimes: gravity-stabilized or unstabilized invasion percolation [16,19,21].

In mobile porous media, however, the coupling between the dynamics of the invading/defending fluids and grain motion is complex. Modeling this coupling is not only computationally demanding but also remains an open field of research [22]. Nevertheless, these systems can be modeled under certain approximations by considering propagation on a network. The key idea consists in updating the network properties after each gas pathway propagates through the entire system, thus mimicking the actual modification of the granular matrix caused by local particle movements. Although simplistic, when carefully implemented, such models have successfully captured, for instance, the morphology of the gas invasion zone in immersed granular media [23,24].

In many real-world scenarios, fluid injection into porous media may occur repeatedly over time. Under these conditions, pathways created by earlier invasions directly influence subsequent ones. Such *memory effects* arise from alterations in the local capillary pressure field due to previous invasions, thereby establishing preferential routes for subsequent fluid migration. Once a fluid pathway is established, local heterogeneities are affected in such a way that it leaves behind a preferential path that later invasions are more likely to follow. This feedback mechanism causes repeated fluid migrations to retrace or reinforce existing pathways, ultimately reshaping the overall percolation pattern over multiple injection cycles. However, only a few works have considered memory effects in invasion percolation problems. A fundamental study focusing on the problem of finding the path that minimizes the sum of thresholds in a two-dimensional (2D) square lattice has demonstrated that this rule assigns long-term memory to the invasion front, with a direct connection to invasion percolation in a gradient [25]. More recently, an experimental

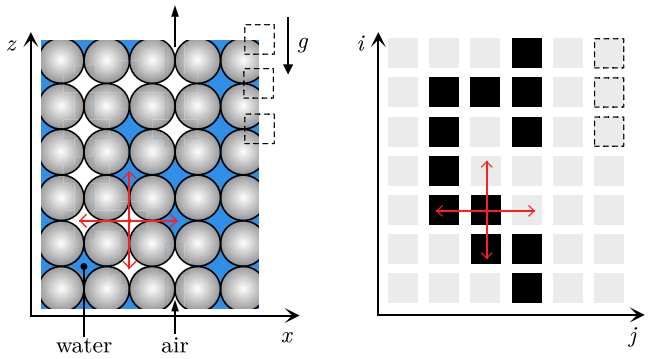

FIG. 1. (Left) Schematic of the grain arrangement and gas propagation through the porous structure. At each pore, the gas has four possible directions to invade, indicated by red arrows. (Right) Matrix representation of the same configuration. Outlined squares indicate the reference position of specific pores, serving as a visual guide between the two panels. Black squares mark the pores already invaded by the gas, while gray squares denote available (yet uninvaded) sites.

study on cyclic fluid displacement in a disordered medium with an effective gravity has pointed out the emergence of hysteresis and memory in the front propagation [26]. Previous studies have shown the importance of quantifying and predicting localized fluid injection and propagation in a disordered medium submitted to a pressure gradient [23,24,27]. These studies demonstrated that, in this configuration, repeated invasion pathways lead to a global invasion zone characterized by contours well-described by a diffusionlike process [23]. However, to our knowledge, no work has considered the effect of memory in such a problem.

This work considers immiscible fluid propagation in a disordered porous medium in the presence of gravity—for instance, gas rising in an immersed granular medium. Its originality lies in considering a localized fluid injection rather than a front propagation, and to include a history-dependent or memory term. This simple numerical model is able to capture the main features of memory-driven path selection. By adjusting a parameter that weights the impact of prior percolation events, we investigate how gas pathways stabilize, branch, or shift when varying the intensity of the memory effects.

II. NUMERICAL APPROACH

Following the approach presented in [23,24], we model the system as a two-dimensional matrix, in which each matrix element represents the void space between four grains (Fig. 1). The matrix dimensions (515 × 651; height × width) are chosen sufficiently large to minimize boundary effects and ensure the formation of well-defined percolation paths. Each node (i, j) is initially implemented with two contributions: (i) a capillary overpressure representing the threshold to overcome for the gas to propagate through this pore (node); this capillary overpressure is drawn from a Gaussian distribution with standard deviation σ_P representing local heterogeneities; (ii) a linear pressure gradient δp_h, representing the hydrostatic pressure gradient due to gravity [Fig. 2(a)]. At the beginning of each iteration k, gas is locally injected from a central point at the bottom boundary of the matrix [Fig. 2(b), starting point for $k = 1$]. Previous studies suggest that air propagation in such systems can be characterized as a diffusive process with an effective diffusion coefficient $D = D(\chi)$, where the dimensionless parameter $\chi = \sigma_P/\rho g d$ quantifies the ratio between the standard deviation σ_P of the capillary overpressure distribution at the pore scale and the characteristic hydrostatic pressure variation $\rho g d$ across a grain diameter d [23,24,28]. Consequently, the advancement of the air path is governed by the local capillary heterogeneity, represented by $\delta p_c(\sigma_P)$, and by the net pressure difference $\delta p_t = \delta p_c(\sigma_P) - \delta p_h$, which encapsulates the interplay between capillary and hydrostatic

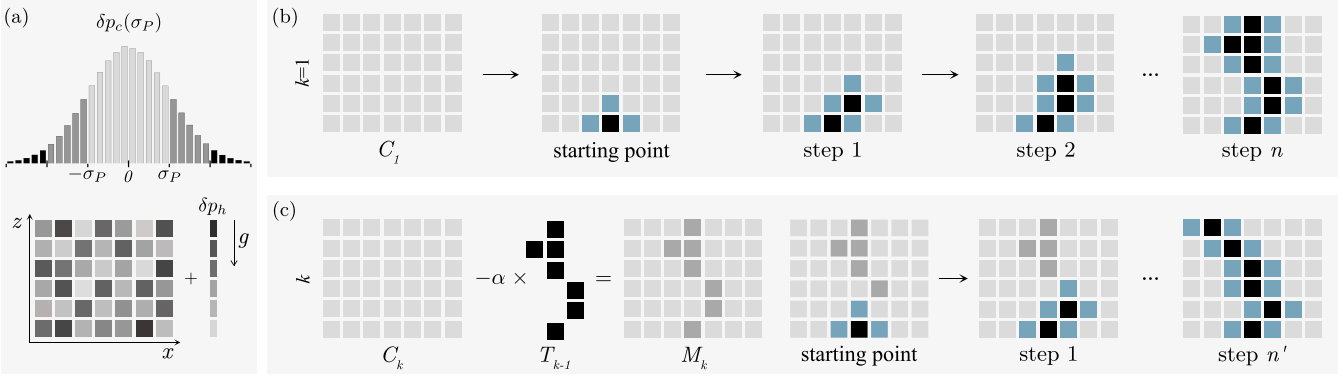

FIG. 2. Illustration of the percolation path simulation process. (a) The porous medium is modeled as a two-dimensional square lattice (bottom). Each node is assigned a capillary overpressure threshold drawn from a normal distribution centered at zero with standard deviation $\sigma_P = 1$, representing the distribution of capillary overpressure thresholds $\delta p_c(\sigma_P)$ (top). After each path, the lattice is reinitialized with new values sampled from the same distribution. In addition, a linear pressure gradient δp_h is added, generating the initial condition C_k (bottom). Memory effects are added from the second path on [see (c)]. (b) Example of the first invasion ($k = 1$). The panel displays the initial condition C_1, the starting point, and the iterative progression. The percolation path (in black) advances by selecting, among the neighboring cells (light blue), the one with the minimum pressure. The path ends when reaching the top row (here, after n iterations). (c) Example of a subsequent pathway ($k > 1$). The memory from the previous invasion $k - 1$ is imposed by subtracting α from every cell $T_{k-1}(i, j)$ visited in the previous trajectory, yielding $M_k = C_k - \alpha T_{k-1}$ (light gray cells). Each path ends upon reaching the top row (here, after n' iterations). The procedure is repeated for each subsequent pathways.

pressures. In all simulations, we set $\chi = 140$ to ensure an extensive lateral exploration of the medium and to facilitate a rigorous assessment of memory effects on the system's evolution.

The simulation starts by initiating the percolation process from the starting point through the matrix $C_{k=1}(i, j)$ consisting of both contributions of the capillary threshold overpressure distribution and the hydrostatic pressure gradient [Fig. 2(a)]. At each iteration, the advancing path is determined by selecting, among the four nearest neighbors (up, down, left, right), the cell with the minimum pressure value [Fig. 2(a), light blue cells]. This procedure effectively mimics the preferential flow of air through regions of minimal resistance within an immersed porous medium in a gravity field. The first gas pathway ($k = 1$) stops when reaching the top row [Fig. 2(b), right]. At the beginning of each subsequent gas pathway ($k > 1$), a new matrix $C_k(i, j)$ is generated [Fig. 2(c)], whose elements represent the capillary threshold overpressures redrawn from the same normal distribution [Fig. 2(a), up], to which the hydrostatic pressure gradient is added again [Fig. 2(a), down]. In addition, to account for memory effects, a history term weighted by the parameter α is introduced, which biases the trajectory based on the previously explored path $(k - 1)$. The matrix through which we consider the percolation process for the path k is therefore defined as

$$M_k(i, j) = \begin{cases} C_1(i, j), & k = 1, \\ C_k(i, j) - \alpha\, T_{k-1}(i, j), & k \geqslant 2, \end{cases} \tag{1}$$

where T_{k-1} is the track followed by the gas in the previous iteration, defined as $T_{k-1}(i, j) = 1$ if the cell was part of the $(k - 1)$th gas pathway, and $T_{k-1}(i, j) = 0$ otherwise. The parameter α represents a constant pressure value subtracted from previously invaded sites. Given that the typical pressure fluctuations in the matrices C_k have a standard deviation of unity, varying α from 0 (no memory) up to 4 (strong memory) effectively tunes the strength of memory effects relative to the characteristic pressure scale of the system. By subtracting α at these locations, the matrix M_k retains a memory of the prior trajectory [Fig. 2(c), light gray cells], thereby favoring continuity and mitigating abrupt deviations in subsequent path selections. Similarly to $k = 1$, the iterative process for each subsequent path k ends once the percolation path reaches the top row of the matrix [Figs. 2(b) and 2(c), right images]. For each value of α, we run the simulation for N subsequent pathways. Unless specified, in the following, $N = 5000$.

Figure 3 displays the effect of the memory term by comparing two consecutive channels. In the absence of memory ($\alpha = 0$), only sporadic overlaps are observed near the injection point—a consequence of random intersections between independent paths. As the memory parameter increases, three key phenomena emerge: (i) an increased number of repeated paths, (ii) a tendency for overlap regions to be retraced, particularly in the vertical direction, and (iii) a progressive localization of the channel, leading to reduced lateral exploration. These cumulative effects give rise to characteristic percolation structures, which will be discussed in detail in the following section.

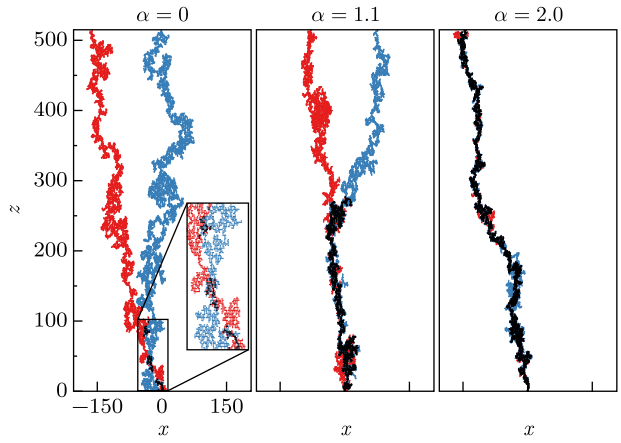

FIG. 3. Two successive paths, T_k (dark red) and T_{k+1} (light blue), are shown for different values of memory α. The overlap between consecutive trajectories is highlighted in black. As α increases, paths increasingly retrace previously explored channels, making the overlap more pronounced. In the absence of memory ($\alpha = 0$), overlaps occur only sporadically, forming isolated clusters (zoom in inset).

III. RESULTS

In this section, we first analyze the global behavior of the system by examining the cumulative effect of multiple simulated gas pathways, distinguishing between total trajectory density and local overlaps between successive pathways (see Sec. III A). We explore specifically how varying the strength of the memory parameter influences the persistence of initially imposed conditions throughout subsequent invasions. Next, we investigate local statistical characteristics of the trajectories (Sec. III B), highlighting differences in dynamics and statistical distributions between newly explored and repeatedly visited regions. Finally, we perform a morphological analysis (Sec. III C), quantifying how memory effects shape the overall orientation and spatial organization of gas pathways.

A. Global morphology

To characterize the overall shape and pattern resulting from the superposition of individual percolation paths, we define two normalized quantities: the cumulative path density $\rho_c(x, z)$ and the overlap density $\rho_o(x, z)$. These metrics represent, respectively, the total accumulation of trajectories and the regions shared by successive paths. Their mathematical definitions, normalized by the total number of iterations N, are given by

$$\rho_c = \frac{1}{N} \sum_k T_k \,, \tag{2}$$

$$\rho_o = \frac{1}{N} \sum_k (T_k \odot T_{k+1}), \tag{3}$$

where $\odot$ denotes the Hadamard matrix product, corresponding to the elementwise matrix multiplication, $(T_k \odot T_{k+1})_{ij} = (T_k)_{ij}(T_{k+1})_{ij}$.

Figure 4 shows the results for different values of the memory parameter α. The first noticeable effect is that increasing the influence of the previous path stabilizes the air channel.

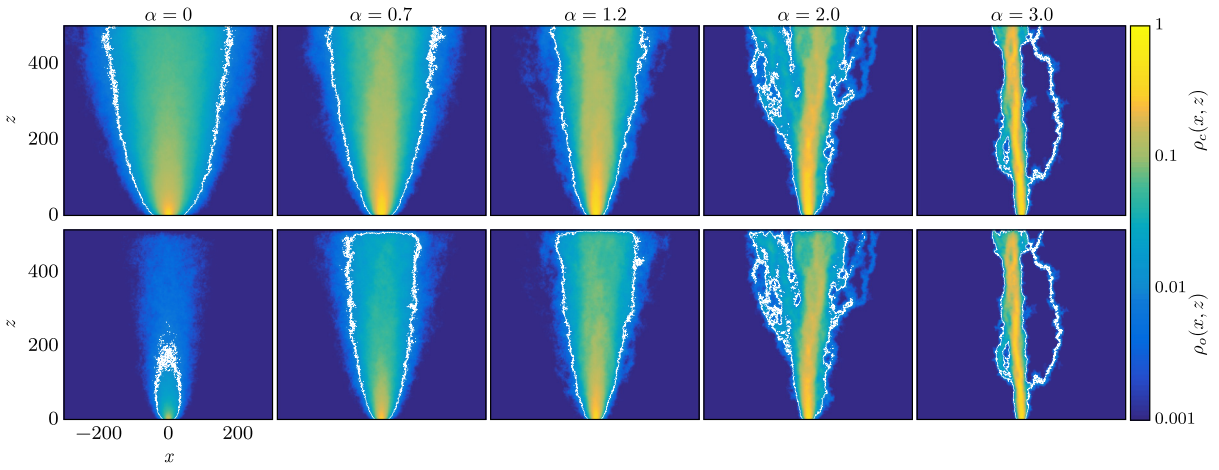

FIG. 4. Global morphology for $N = 5000$ trajectories as a function of the memory parameter α. (Top row) Cumulative path density, $\rho_c(x, z)$ [Eq. (2)]. As the memory weight α increases, the percolation channel becomes narrower, and the formation and stabilization of lateral branches become increasingly pronounced. (Bottom row) Overlap density, $\rho_o(x, z)$ [Eq. (3)], representing the history of the system. The evolution of history, on average, progresses from the injection point at the bottom and gradually loses its symmetry as the air channel stabilizes. For a high memory value ($\alpha = 3$, right images), both densities ρ_c and ρ_0 exhibit similar patterns. Indeed, the initial percolation path dominates the process, regardless of the different pressure distribution on the network from one iteration to the other. The white contour line corresponds to the threshold of 1%, beyond which density values become negligible.

In the absence of memory ($\alpha = 0$), the cumulative density is broadly distributed (Fig. 4, top left image) and the associated movement is diffuse, whereas the overlap density remains low and is confined near the injection point (Fig. 4, bottom left image). As the memory weight increases, the lateral exploration diminishes, yielding narrower density distributions dominated by specific lateral branches (Fig. 4, top panel). Simultaneously, the overlap density grows in magnitude and progressively converges towards the cumulative density (Fig. 4, bottom panel). This behavior is attributed to the fact that as consecutive paths become increasingly similar, their difference remains nearly constant.

Influence of the initial condition

Since the simulation incorporates a memory effect across multiple realizations, the choice of the initial condition is, in principle, significant. To assess the influence of the first generated path on subsequent trajectories, we examine the evolution of two predefined initial conditions: (i) a straight vertical path connecting the virtual injection point to the surface, and (ii) a zigzag path exhibiting a square pattern (Fig. 5, left column). These trajectories are composed of vertical and horizontal straight lines due to the restriction imposed by the identification algorithm, which exclusively selects lateral neighbors under a four-neighbor connectivity scheme (see Sec. II), thereby precluding the detection of diagonal neighbors in subsequent iterations.

Figure 5 illustrates the evolution of the cumulative path density, $\rho_c(x, z)$, over a series of iterations $N = [1, 10, 100, 1000, 3000, 5000]$ for four distinct values of the memory parameter, $\alpha = [0.4, 1.2, 2, 3]$. Regardless of the initial condition, for $\alpha < 2$, the initial trajectory rapidly loses its characteristic structure within approximately the first 100 iterations. In contrast, for $\alpha \geqslant 2$, the initial invasion structure persists over a larger number of iterations ($\approx$3000), although it eventually transitions into a final pattern, losing the memory of the first path. For high memory values ($\alpha = 3.0$), we also tested a more pronounced zigzag path as an initial condition (Fig. 5, last line of the bottom panel). Despite its significant difference from the two other initial conditions, we observe that the system also loses memory of this initial path when the number of iterations becomes sufficiently large. A supplemental movie [29] illustrates the evolution of both of the initial conditions for the four memory values shown in Fig. 5.

Overall, these findings indicate that, even when simulations start from different initial configurations, their subsequent evolution converges into statistically similar patterns. Notably, the initial number of explored events along the first imposed path ($N_i = 515$ and 915 for a vertical and zigzag line, respectively) is rapidly erased and significantly increases by the second iteration ($\sim$7000 visited points for $\alpha = 0.4$ and $\sim$4000 for $\alpha = 3$). This suggests that the system quickly explores a broad set of new neighboring sites, leading to the immediate loss of memory of the initial condition, regardless of the imposed trajectory. Importantly, these results highlight that even for large memory values, the influence of the initial pathway remains transient. This observation is further corroborated in the next section, where we analyze the properties of local trajectories to gain deeper insight into how memory influences path selection.

B. Local trajectories

To gain deeper insight into the local dynamics, we plot in Fig. 6, as a function of the iteration number k, the number of points $N_c(k)$ explored by the current trajectory T_k, along with the number of repeated (or overlapping) points $N_r(k)$ between T_k and T_{k-1}. In the absence of memory [Fig. 6(a), $\alpha = 0$], N_c and N_r fluctuate over time with no discernible correlation. As α increases, a correlation emerges between the two signals, such that variations in one are reflected in the other [Fig. 6(a),

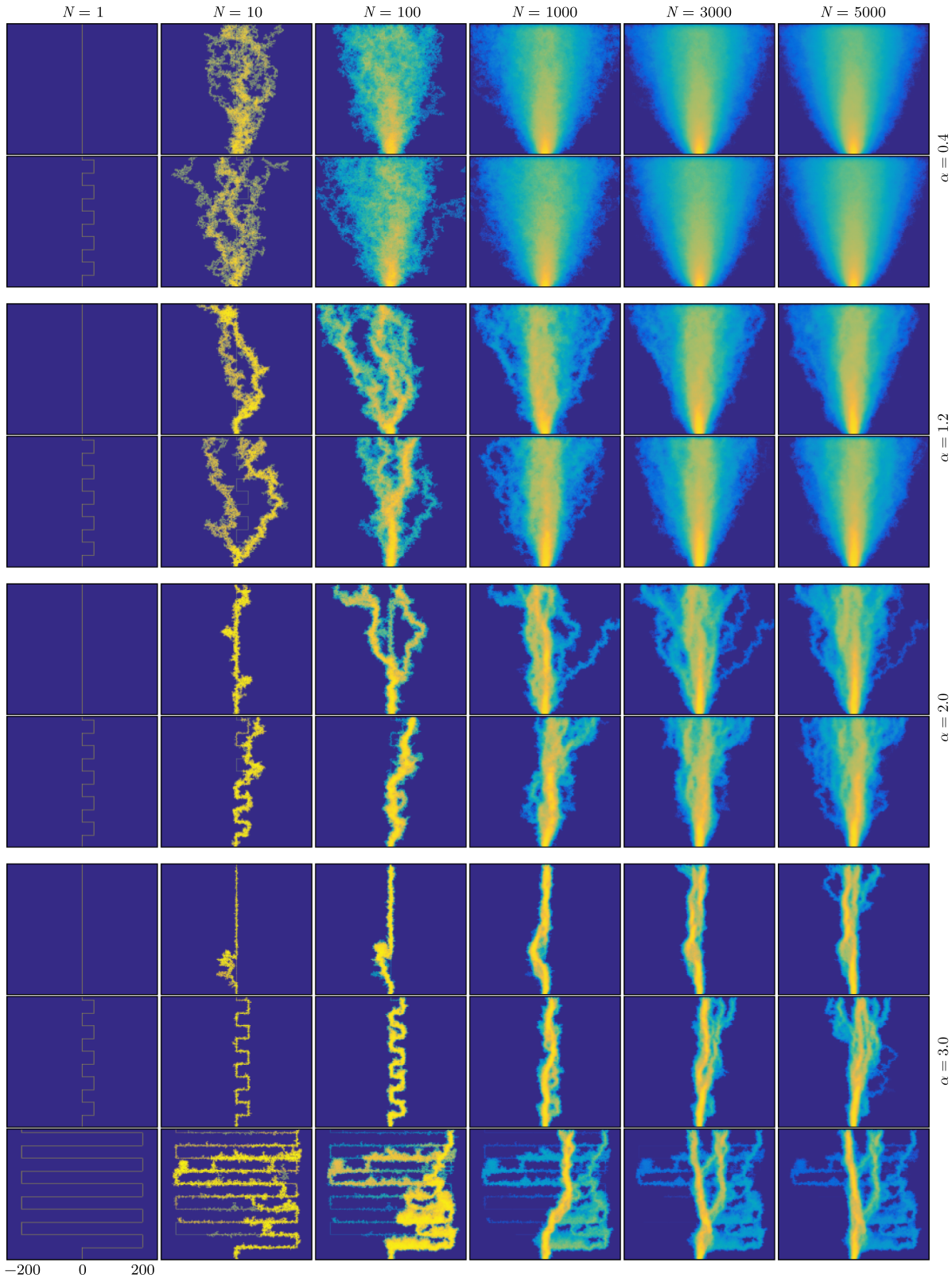

FIG. 5. Evolution of the cumulative path density $\rho_c(x, z)$ as a function of the iteration number N, for two different imposed initial paths (of length N_i, see the left column): a vertical line ($N_i = 515$) and a square-pattern zigzag ($N_i = 915$). The top, central, and bottom panels display the results for different memory values α. For high memory ($\alpha = 3.0$, bottom panel), a more pronounced zigzag has been tested ($N_i = 4315$, bottom line, see text). Color bar is the same as in Fig. 4.

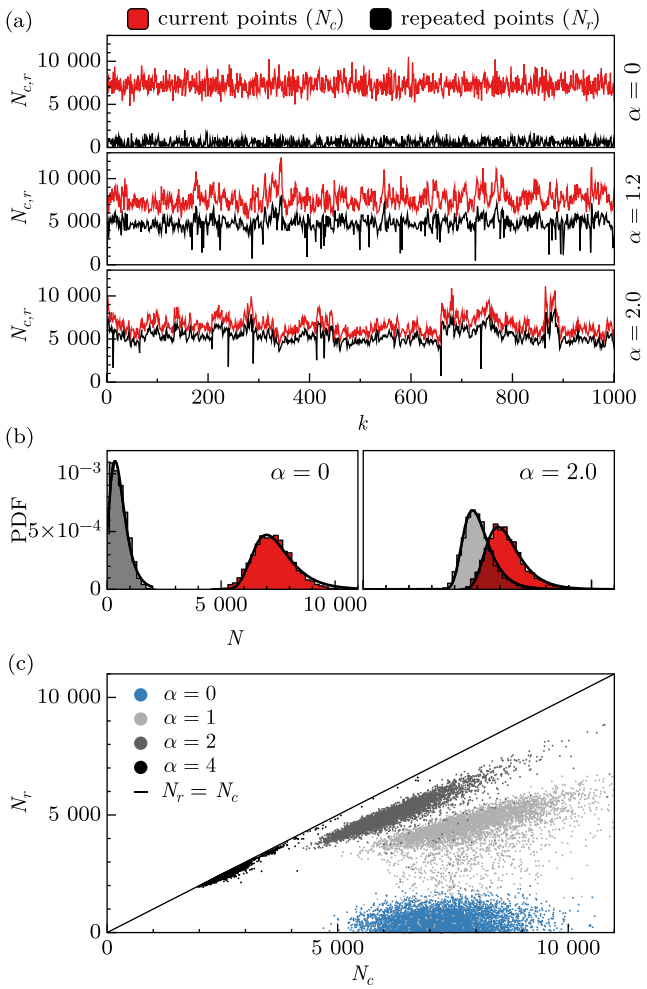

FIG. 6. Statistical characterization of local trajectories. (a) Number of visited points for the current path, $N_c(k)$ (in red), and the repeated points, $N_r(k)$ (in black), as a function of the iteration number k for different values of α. When α increases, N_c and N_r converge toward each other. (b) Probability density functions (PDFs) of N_c (red) and N_r (gray) for no memory ($\alpha = 0$, left) and strong memory ($\alpha = 2$, right). Both distributions are asymmetric, skewed toward lower values, and well-fitted by a Gumbel distribution (solid black lines). (c) Scatter plot showing the relationship between repeated points N_r and current points N_c. Without memory, these quantities are uncorrelated. With increasing α, correlation strengthens, eventually converging onto the line $N_r = N_c$ for large memory ($\alpha = 4$).

$\alpha = 1.2$]. Moreover, when the influence of the previous path becomes stronger, N_c and N_r converge [Fig. 6(a), $\alpha = 2.0$]. The figure also shows that repeated trajectories undergo sharp drops at specific moments (indicated by vertical black lines). These abrupt decreases occur when the path suddenly deviates and no longer follows its predecessor (see the supplemental video [29]). However, such deviations become increasingly rare as the memory weight α grows.

Figure 6(b) illustrates the probability density function (PDF) of N_c (red) and N_r (gray) for the no-memory case ($\alpha = 0$, left panel) versus the high-memory case ($\alpha = 2.0$, right panel). The distribution of the repeated points is narrower than that of the current path, and it is also shifted to lower values,

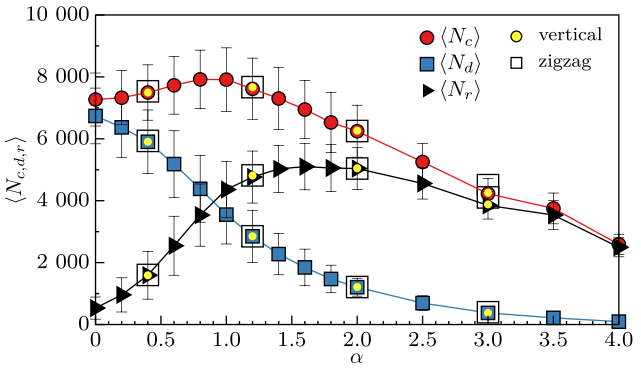

FIG. 7. Average values, computed over N iterations, for the number of points per trajectory ($\langle N_c \rangle$, red circles), the number of repeated points ($\langle N_r \rangle$, black triangles), and the number of newly explored points that were not part of the previous trajectory ($\langle N_d \rangle$, blue squares). As the memory parameter α increases, the difference between consecutive trajectories decreases, and the number of repeated invaded points converges to that of the original trajectory. A critical transition occurs near $\alpha \approx 1$, where repeated points start to dominate new explorations. Yellow dots and white squares correspond to data from two different initial conditions (a vertical line and a square-pattern zigzag).

resulting in a systematically smaller average. Both PDFs are asymmetric and exhibit light tails, and they can be fitted using a Gumbel distribution:

$$f(x) = \frac{1}{\beta} \exp\left[-(z + e^{-z})\right], \tag{4}$$

where $z = (x - \mu)/\beta$, μ is the mean, and β is the scale parameter controlling the spread of the distribution. The solid black lines in Fig. 6(b) represent fits to the PDFs using the Gumbel distribution given in Eq. (4). It is worth noting that although the original pressure distribution in the medium is Gaussian, the process of selecting local minima to determine the trajectory T_k effectively transforms it into a Gumbel distribution, reflecting the nonlinear nature of path selection.

Figure 6(c) shows the overall correlation between the repeated points, N_r, and the total number of visited points in the current path, N_c. In the absence of memory ($\alpha = 0$, blue points), these two variables are uncorrelated. As α increases (light and dark gray points), their scatter is reduced and they become progressively more correlated. For very large memory values ($\alpha = 4$, black points), N_r converges toward N_c, causing the data points to align on the line $N_r = N_c$.

We now analyze the average number of points associated with three variables: the current path $\langle N_c \rangle$, the difference between two consecutive paths $\langle N_d \rangle$, and the repeated path $\langle N_r \rangle$. By construction, the current path consists of both new (difference) and repeated components, i.e., $N_c = N_d + N_r$. Figure 7 summarizes the evolution of these quantities as a function of α. Initially, $\langle N_c \rangle$ increases and reaches a maximum at approximately $\alpha \approx 1$, after which it gradually decreases. In contrast, the number of repeated points, $\langle N_r \rangle$, steadily grows until it eventually matches N_c, while the number of new points, $\langle N_d \rangle$, continually declines. A critical point emerges around $\alpha \approx 1$, where $\langle N_d \rangle$ and $\langle N_r \rangle$ become comparable.

Additionally, Fig. 7 shows results for different initial conditions. Notably, whether the trajectory starts as a zigzag path (and hence contains more points) or as a straight vertical path, subsequent iterations converge to a similar range in all cases. This observation illustrates the self-regulating nature of the percolation process, in which the influence of the initial condition diminishes as the system evolves. The critical value $\alpha = 1$ is directly tied to the capillary overpressure $\sigma_P = 1$ used in the simulations, as it represents the threshold at which memory effects begin to dominate. Specifically, when $\alpha > \sigma_P$, the imposed memory exceeds the pore-size distribution width, favoring a preferential path selection that effectively overrides local variations in the immediate neighborhood.

C. Path orientation

Finally, we focus on the morphology and orientation of the gas trajectories by quantifying how their preferred direction evolves as a function of the memory strength α. To this end, each trajectory is analyzed geometrically by fitting an equivalent ellipse characterized by a centroid and major/minor axes [Fig. 8(a)]. The orientation angle θ of each fitted ellipse is then defined relative to the vertical axis.

In the absence of memory ($\alpha = 0$), paths exhibit a clear vertical symmetry ($\langle\theta \approx 0\rangle$), reflecting unbiased propagation predominantly aligned with the gravity-induced pressure gradient. As α increases, the symmetry breaks progressively, resulting in trajectories with increasingly inclined orientations [Fig. 8(b)]. Such a shift indicates that paths become more constrained and biased, progressively retracing and reinforcing specific preferred channels across multiple invasions.

The temporal evolution of the orientation angle θ transitions from a highly variable distribution at low memory ($\alpha \approx 0$) toward stabilization on specific paths at larger values of α, separated by large jumps [Fig. 8(c)]. To further quantify the lateral confinement of the trajectories, we compute the horizontal accumulation defined as

$$n_x(x,k) = \frac{1}{N}\sum_z \rho_c(x,z), \tag{5}$$

where N is the total number of iterations. $n_x(x,k)$ represents the vertical average of cumulative trajectories across the horizontal axis. The spatiotemporal diagram of n_x is represented in Fig. 8(d) for different values of α. The evolution of the orientation angle θ, superimposed on the panels (white line), reveals a clear correlation with the predominant orientation of the trajectory.

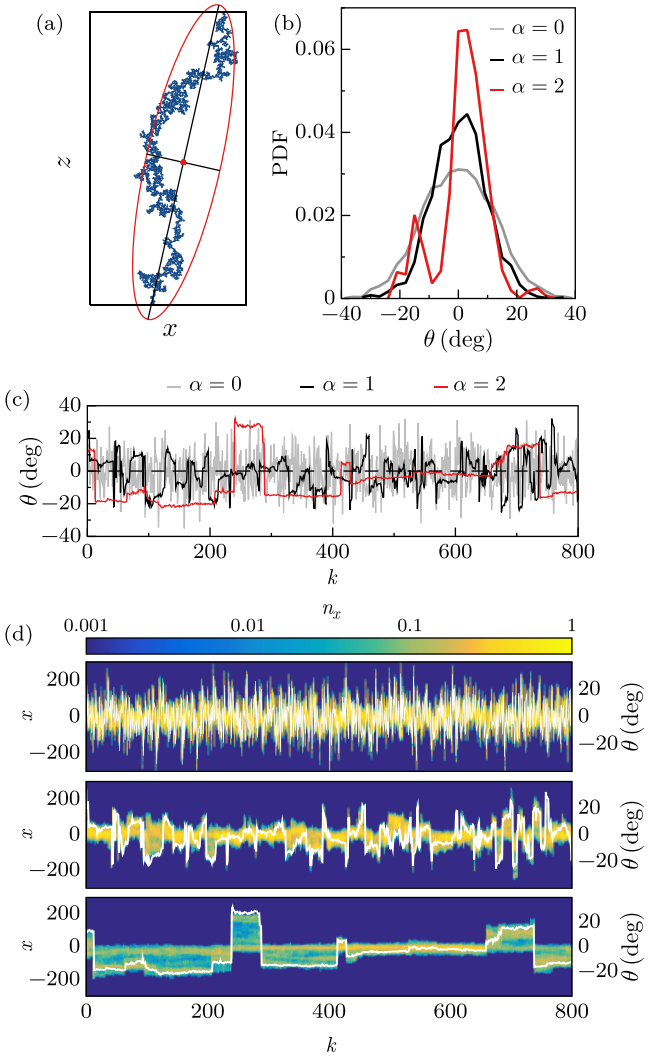

FIG. 8. Morphological analysis of a trajectory. (a) Each trajectory (in blue) is treated as a single object for calculating geometric properties. An ellipse (in red) is fitted to quantify the orientation angle θ with respect to the vertical axis. (b) Probability density function (PDF) of the orientation angle θ for three values of α. When the memory increases, trajectories transition from a symmetric exploration around the vertical to a stabilization towards a single percolation channel at a specific angle. (c) Evolution of the orientation angle for different values of α. For low memory values, the angle exhibits high-frequency variations, which gradually stabilize as the memory effect increases. (d) Spatiotemporal diagram of the horizontal cumulation, n_x. n_x correlates with the system's orientation, as indicated by the overlaid white line (from top to bottom, $\alpha = 0, 1, 2$).

IV. DISCUSSION

In this section, we explore the statistical properties governing the selection process between new and previously visited sites. As previously mentioned, the number of points in the current path N_c and the number of repeated points between successive trajectories N_r follow distributions whose minima are well described by Gumbel distributions [Fig. 6(b)]. We define the probability $P(\alpha)$ as the ratio between the average number of repeated points N_r and the total number of visited points N_c per trajectory:

$$P = \frac{\langle N_\mathrm{r}\rangle}{\langle N_\mathrm{c}\rangle}, \tag{6}$$

thus quantifying the bias toward revisiting previously occupied paths. To describe its dependence on the memory parameter α, we adopt a logistic functional form:

$$P(\alpha) = \frac{1}{1+\exp\left(\frac{\alpha-\alpha_0}{s}\right)}, \tag{7}$$

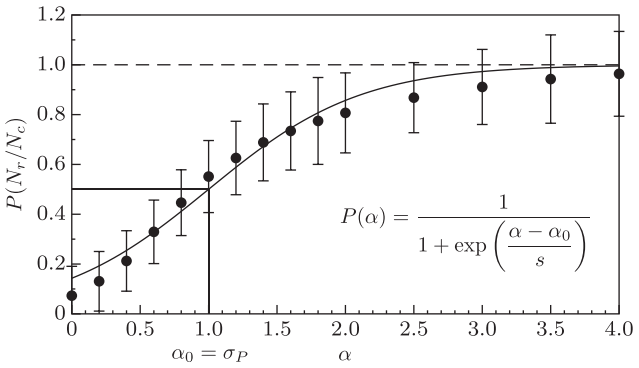

FIG. 9. Probability $P(\alpha)$ of selecting repeated sites as a function of the memory parameter α. Symbols represent the numerical data, and the solid line indicates the fit by a logistic function [Eq. (7)] with a sharpness $s \approx 0.56$. The crossover $\alpha_0 \simeq \sigma_P = 1$ marks a balanced selection (50%) between repeated and new sites.

where α_0 is the characteristic memory strength at which there is equal probability (50%) of selecting either repeated or new sites, and s characterizes the sharpness of this transition. Note that, although extreme value theory demonstrates that the difference between two independent Gumbel-distributed random variables follows a logistic distribution, here we empirically adopt the logistic functional form as a phenomenological fit to quantify the probability $P(\alpha) = \langle N_r \rangle / \langle N_c \rangle$. This ratio directly measures the probability of reinvasion and effectively characterizes the relative shift between distributions associated with opening new pores versus reinvading previously opened ones.

Figure 9 shows the probability $P(\alpha)$, computed from our numerical model (symbols) and the fit with the logistic model from Eq. (7). The function captures well the data, with $\alpha_0 = 1.0 \simeq \sigma_P$ and a sharpness $s \approx 0.56$. Notably, the condition $P(\alpha = 0) = 0.5$ does not generally hold due to asymmetries in the number of visited versus unvisited sites available at each step. In our simulations, the crossover occurs $\alpha_0 \simeq \sigma_P = 1$, indicating that a moderate memory effect is required to achieve equal likelihood (50%) of selecting repeated versus new sites. Furthermore, even without memory ($\alpha = 0$), the observed probability does not start at 0 but exhibits a baseline determined by the intrinsic probability of random overlaps, leading typically to a probability less than 0.1. This baseline reflects the intrinsic spatial correlation among trajectories resulting from their stochastic intersections, estimated to be approximately 0.08 in our simulations. Although this intrinsic overlap probability could depend on the parameter χ, which controls the lateral dispersion of trajectories, a detailed exploration of this relationship is beyond the scope of this work.

At high memory strength ($\alpha > 3$), the selection probability approaches unity (around 90%), significantly enhancing repeated visits and reinforcing stable percolation paths. This regime demonstrates a strong memory effect, effectively confining gas trajectories within established preferential channels.

V. CONCLUSION

This study analyzed the impact of memory effects on gas percolation dynamics within a water-saturated porous medium through a simplified two-dimensional numerical model. Our approach introduces a memory term that modulates the percolation pathways by preferentially weighting previously invaded sites, thereby reflecting the history-dependent nature of the process. We systematically investigated the role of the memory parameter α, observing how it shapes the spatial distribution and morphology of the gas invasion pathways.

Increasing the memory parameter progressively confines gas paths into fewer, more clearly defined channels. At high memory values, gas preferentially revisits previously established pathways, leading to stable and persistent channels dominating local random capillary threshold fluctuations.

We observed that initially imposed conditions temporarily influence path development, but their effects rapidly diminish with subsequent iterations. Consequently, simulations initialized with distinctly different invasion patterns ultimately converge toward statistically similar global configurations. This transient influence underscores the self-organizing characteristic of memory-driven percolation dynamics, highlighting the robustness of channel formation against initial perturbations.

Statistical analyses of trajectory data reveal that the distributions of the explored points follow a Gumbel distribution, due to the nonlinear selection of pressure minima. Furthermore, a logistic function accurately describes the probability of selecting previously invaded sites, indicating an apparent threshold behavior driven by the interplay between memory strength and local heterogeneities. Importantly, even without explicit memory (i.e., $\alpha = 0$), we found a baseline repetition probability arising from inherent random intersections between independent pathways.

These findings collectively demonstrate how memory effects significantly shape gas percolation patterns, underscoring the importance of considering historical interactions in multiphase flow models in porous media. Future investigations could extend this analysis by exploring three-dimensional scenarios, multiple injections where interactions between air channels occur [30], or incorporating more complex pore-scale interactions to enhance the model's realism and predictive power.

ACKNOWLEDGMENTS

The authors gratefully acknowledge the anonymous referees for insightful comments and valuable suggestions, which significantly contributed to improving the manuscript.

DATA AVAILABILITY

The data that support the findings of this article are not publicly available upon publication because it is not technically feasible and/or the cost of preparing, depositing, and hosting the data would be prohibitive within the terms of this research project. The data are available from the authors upon reasonable request.

[1] F. A. L. Dullien, *Porous Media: Fluid Transport and Pore Structure*, 2nd ed. (Academic Press, San Diego, 1992).
[2] M. Sahimi, Rev. Mod. Phys. **65**, 1393 (1993).
[3] K. R. Reddy, S. Kosgi, and J. Zhou, Hazard. Waste Hazard. Mater. **12**, 97 (1995).
[4] R. Semer, J. A. Adams, and K. R. Reddy, Geotech. Geol. Eng. **16**, 59 (1998).
[5] H. Svensen, S. Planke, A. M.-S. Renssen, B. Jamtveit, R. Myklebust, T. R. Eidem, and S. S. Rey, Nature (London) **429**, 542 (2004).
[6] H. Svensen, S. Planke, L. Chevallier, A. M.-S. Renssen, F. Corfu, and B. Jamtveit, Earth Planet. Sci. Lett. **256**, 554 (2007).
[7] S. S. S. Cardoso and J. H. E. Cartwright, Nat. Commun. **7**, 13266 (2016).
[8] K. R. Reddy and J. A. Adams, J. Geotech. Geoenviron. Eng. **127**, 234 (2001).
[9] D. Wilkinson and M. Barsony, J. Phys. A Math. Gen. **17**, L129 (1984).
[10] M. Eden, in *Proceedings of the Fourth Berkeley Symposium on Mathematical Statistics and Probability*, edited by J. Neyman (University of California, Berkeley, CA, 1961), Vol. 4, pp. 223–239.
[11] T. A. Witten and L. M. Sander, Phys. Rev. Lett. **47**, 1400 (1981).
[12] T. A. Witten and L. M. Sander, Phys. Rev. B **27**, 5686 (1983).
[13] P. Meakin, J. Colloid Interface Sci. **96**, 415 (1983).
[14] H. Mártin, J. Vannimenus, and J. P. Nadal, Phys. Rev. A **30**, 3205 (1984).
[15] D. Wilkinson, Phys. Rev. A **30**, 520 (1984).
[16] P. Meakin, J. Feder, V. Frette, and T. Jøssang, Phys. Rev. A **46**, 3357 (1992).
[17] M. Chaouche, N. Rakotomalala, D. Salin, B. Xu, and Y. C. Yortsos, Phys. Rev. E **49**, 4133 (1994).
[18] J. Schmittbuhl, A. Hansen, H. Auradou, and K. J. Måløy, Phys. Rev. E **61**, 3985 (2000).
[19] Z. Bo, D. Loggia, L. Xiaorong, G. Vasseur, and H. Ping, Eur. Phys. J. B **50**, 631 (2006).
[20] P. Reis, M. Moura, G. Linga, P. A. Rikvold, R. Toussaint, E. G. Flekkøy, and K. J. Måløy, Adv. Water Resour. **182**, 104580 (2023).
[21] A. Birovljev, L. Furuberg, J. Feder, T. Jøssang, K. J. Måløy, and A. Aharony, Phys. Rev. Lett. **67**, 584 (1991).
[22] M. Constant, N. Coppin, F. Dubois, V. Vidal, V. Legat, and J. Lambrechts, Comp. Part. Mech. **8**, 535 (2021).
[23] G. Varas, V. Vidal, and J.-C. Géminard, Phys. Rev. E **83**, 011302 (2011).
[24] G. Varas, V. Vidal, and J.-C. Géminard, Phys. Rev. E **83**, 061302 (2011).
[25] H. Kharabaf and Y. C. Yortsos, Phys. Rev. E **55**, 7177 (1997).
[26] R. Holtzman, M. Dentz, R. Planet, and J. Ortín, Commun. Phys. **3**, 222 (2020).
[27] G. Varas, G. Ramos, J.-C. Géminard, and V. Vidal, Front. Phys. **3**, 44 (2015).
[28] G. Varas, J.-C. Géminard, and V. Vidal, Granular Matter **15**, 801 (2013).
[29] See Supplemental Material at http://link.aps.org/supplemental/10.1103/d19h-6lx1 for visualization of the path dynamics under different initial conditions.
[30] G. Varas, G. Ramos, and V. Vidal, Phys. Rev. E **110**, 024901 (2024).